
Identification of low energy neutral and charged cosmic ray events in large wide field observatories

L. Apolinário^{1,2}, P. Assis^{1,2}, P. Brogueira^{1,2}, R. Conceição^{1,2,a}, P. J. Costa^{1,2}, G. La Mura^{1,3}, M. Pimenta^{1,2}, B. Tomé^{1,2}

¹LIP - Laboratório de Instrumentação e Física Experimental de Partículas, Lisbon, Portugal

²Departamento de Física, Instituto Superior Técnico, Universidade de Lisboa, Lisbon, Portugal

³INAF - Osservatorio Astronomico di Cagliari, Selargius, Italy

Received: date / Accepted: date

Abstract The lower energy thresholds of large wide-field gamma-ray observatories are often determined by their capability to deal with the very low-energy cosmic ray background. In fact, in observatories with areas of tens or hundreds of thousands of square meters, the number of background events generated by the superposition of random, very low energy cosmic rays is huge and may exceed by far the possible signal events. In this article, we argue that a trigger strategy based on pattern recognition of the shower front can significantly reject the background, keeping a good efficiency and a good angular accuracy (few square degrees) for gamma rays with energies as low as tens of GeV. In this way, alerts can be followed or emitted within time lapses of the order of the second, enabling wide-field gamma-ray observatories to better contribute to global multi-messengers networks of astrophysical observatories.

Keywords gamma-rays · charged cosmic-rays · transients · multi-messengers networks

1 Introduction

The observation of transients in the sky was always a source of great interest, even of astonishment, for the general public and a privileged object of study for scientists. The sky is, in this way, constantly scrutinized by a large number of detectors exploring all possible particle messengers and, in particular, photons within a very wide range of energies. At the gamma-ray energy region, satellite experiments cover the sky up to energies of a few tens of GeV. Above these energies, ground-based observatories assume these obser-

vations. These include Imaging Atmospheric Cerenkov Telescopes (IACT) and Extensive Air Shower (EAS) arrays.

IACTs [1,2,3] exhibit favorable attributes such as low energy thresholds (within the range of a few tens of GeV) and exceptional angular resolution (measured in a few arcminutes). However, they also come with limitations, including a relatively narrow field of view (typically on the order of a few degrees) and lower duty cycles (around 10 - 15%).

Conversely, contemporary EAS arrays [4,5] feature significantly broader fields of view (measured in steradians), along with nearly complete duty cycles, close to 100%. Yet, they are accompanied by certain drawbacks, notably diminished angular resolution (around 1-2 degrees at lower energies) and higher energy thresholds (in the range of a few hundreds of GeV).

In fact, in an array of Water Cerenkov Detectors (WCD), as described below and in an interval of a few hundred nanoseconds, the expected level of signal and background rates (see section 2) will imply several tens of hit stations. Thus, a trigger/analysis strategy, based just on requiring a small number of hit stations, would saturate any sustainable Data Acquisition (DAQ) system and cannot work at lower energy thresholds. To effectively handle the substantial background, a low-energy trigger system must achieve rejection factors within the range of $10^3 - 10^5$. It is important to highlight that without such significant reduction, the data flow would reach an unsustainable bandwidth of gigabytes per second, a scenario untenable for a large-scale gamma-ray array experiment.

The strategy explored in this article is based on the recognition of the space-time correlations of the particles in the shower front arriving at one WCD ground

^ae-mail: ruben@lip.pt

array. In this analysis, the shower front was treated as a planar structure.

The detector under consideration occupies an area of $80\,000\text{ m}^2$ and is positioned at 5200 m above sea level. The array configuration, with a circular shape, was emulated by a two-dimensional histogram with cells with an area of $\sim 12\text{ m}^2$; a correction was applied to account for a Fill Factor (FF) of 80%. Station triggering was governed by a probability function that effectively reproduces the trigger rates observed by the High-Altitude Water Cherenkov (HAWC) observatory, as detailed in Section 2.

In essence, the algorithm designed to trigger individual shower events can be succinctly summarized as follows:

- The arrival time, t_i^0 , of the shower plane in each triggered cell was defined as the time of the first particle detected in the cell;
- The event is characterized by the number, locations and t_i^0 s of its triggered cells;
- The planes defined by the combination of the time and space coordinates of any triplet of triggered cells, were characterized by their unitary normal vectors;
- The direction of the normal vectors were clustered using a QCD jet inspired algorithm;
- The size and the direction of the clustered jet vector were taken as, respectively, the trigger variable and the incoming particle direction.
- The directions of the selected clustered jets are used then to update a cumulative lookup table of sky directions.
- Whenever, there will be an accumulation of candidates in one of the cells of the lookup table, an alert will be emitted.

The structure of this article is outlined as follows: In Section 2, we elaborate on the simulation sets, providing a description thereof, while also estimating the anticipated background and signal rates. Section 3 is dedicated to the development of the trigger concept itself, accompanied by an assessment of its performance. Moving to Section 4, we explore a plausible implementation of this trigger through an FPGA-based system coupled with a microprocessor. Additionally, we briefly present its potential to generate multiple tiers of rapid alerts. Lastly, in Section 5, the use of this trigger strategy in future ground array gamma-ray observatories is discussed.

2 Signal, background and simulations

Charged cosmic rays represent a potentially significant signal for energies surpassing a certain threshold while concurrently constituting a formidable background source for gamma rays. This background emerges from extremely low-energy showers, frequently resulting in the generation of isolated muons at ground level, commonly referred to as *atmospheric muons*.

The rate of the atmospheric particles at 5200 m a.s.l. was estimated, considering a WCD with an area of 12 m^2 , to be of the order of $20 - 30\text{ kHz}$ [6]. Similar rates were obtained by the authors using CORSIKA [7] simulations. Here the simulated showers were sampled at an altitude of 5200 m a.s.l. and considering the magnetic field for the geographic location of the ALMA site [8]. The simulation framework of the LATTES experiment [9] – based on the Geant4 toolkit [10, 11, 12] – was used to simulate the detector response¹. From this simulation exercise, it was verified that the station trigger efficiency was roughly 50% for an electromagnetic energy deposition of 15 MeV, similar to what is quoted in [6] for the nominal trigger efficiency curve of a detector unit, with a scale factor for the photon detection efficiency of one. The rate of the possible dark noise and after-pulses able to trigger the cell (detector) in a 200 ns time window was considered to be small and within the uncertainty of the atmospheric muons estimation.

The probability that one shower secondary particle triggers a cell is, following reference [6], defined as:

$$1 - \exp(-F k E), \quad (1)$$

where k was set to $3.86105 \times 10^{-2}\text{ MeV}^{-1}$, F is a scale factor and E the particle energy in MeV. The parameter $F = 1$ describes the probability to detect at least one photoelectron (p.e) in a station of the central array of the HAWC experiment [4]. In this work, conservatively, F was set to one but it would be possible, if enough computing power is available (see section 4), to increase F and thus lower the energy threshold, at least during a given time interval after external or internal alerts.

The distributions of the number of stations triggered by atmospheric muons in a time window of 200 ns are shown in Fig. 1 (top) for scale factors F of 0.1, 1 and 10. For a scale factor of one, the mean number of background stations is 23. The bottom plot of Fig. 1 shows the corresponding variation of the trigger rate with an increasing threshold on the number of active stations. For a scale factor of one and a minimum number of

¹The station trigger condition requires a minimum of 10 photoelectrons.

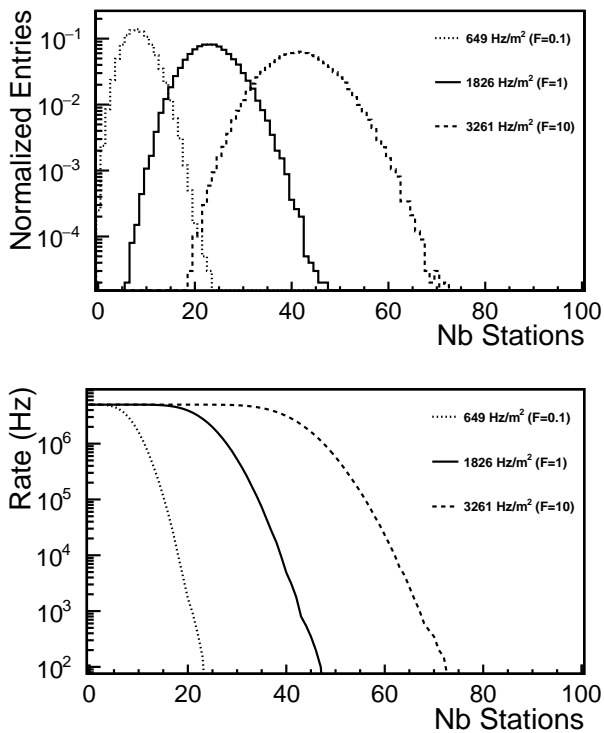


Fig. 1 (top) Number of active stations in 200 ns for different cosmic-ray particle detection rates at 5200 m altitude, corresponding to scale factors $F = 0.1, 1$ and 10 . (bottom) The corresponding rate of triggers on the cosmic-ray background as a function of the minimum number of active stations.

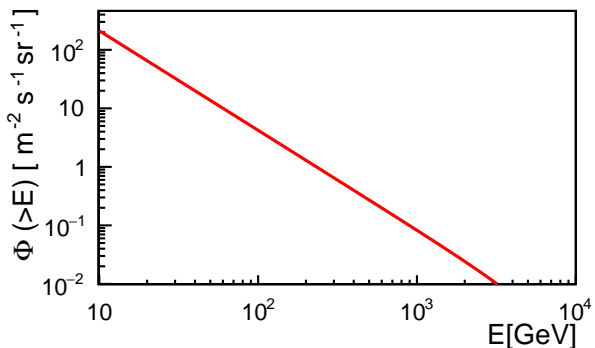


Fig. 2 Integrated charged cosmic-rays flux with energies higher than a given energy (E) as a function of the cosmic ray energy.

active stations lower than 20, the trigger is saturated, corresponding to a trigger rate of 5 MHz.

The integrated flux of charged cosmic rays, with energies higher than a given energy E , is illustrated in Fig. 2 as a function of E . Assuming a field of view of 2 sr, the rate of charged cosmic rays hitting the array with an energy greater than 100 (200) GeV is about 500 (130) kHz.

The gamma and proton-induced shower simulations used in this work were produced using CORSIKA (version 7.5600) [7], taking FLUKA [13,14] and QGSJet-

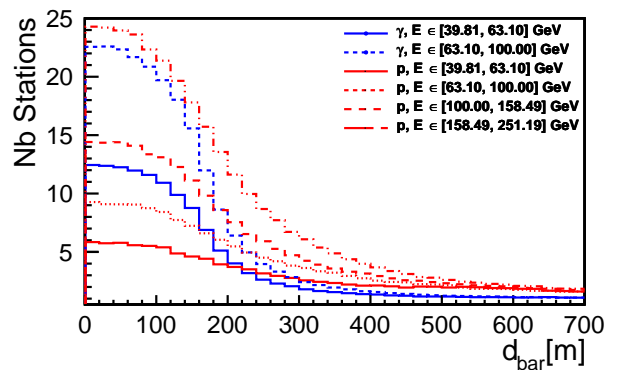


Fig. 3 Mean number of active stations at 5200 m a.s.l as a function of the distance of the events reconstructed core to the centre of the array (d_{bar}), for gamma ray events with a primary energy of about 50 and 80 GeV (blue lines); the red lines represent the corresponding distributions for charged cosmic rays for primary energies of about 50, 80, 130 and 200 GeV.

II.04 [15] as the low- and high-energy hadronic interaction model, respectively. The simulated events were sampled at an altitude of 5.2 km a.s.l., with the shower core randomized uniformly within the array area. The energies were chosen to be between 10 and 250 GeV for gamma and proton-induced showers. The zenith angle θ was set to 10° or 30° , and the azimuthal angle ϕ followed a uniform distribution.

The distributions of the mean number of triggered stations in gamma-ray events with primary energies of about 50 and 80 GeV are shown in blue in Fig. 3 as a function of the distance of the events reconstructed core to the centre of the array, d_{bar} . For d_{bar} lower than 160 m (the array radius), the mean number of triggered stations is between 16 and 24 (80 GeV) and between 9 and 12 (50 GeV). In the same figure, the equivalent distributions for charged cosmic rays of energies of about 50, 80, 130, and 200 GeV are depicted in red. From this figure, it can be concluded that the energies corresponding to the same order of triggered stations are about two times higher in charged cosmic rays than in gamma rays in events where the shower core is lower than 160 m.

The background events from atmospheric muons were generated by randomly selecting stations within the array and assigning arrival times uniformly distributed within the specified time window. The average number of background stations for this array configuration was 23, and for each shower event, this quantity fluctuated according to a Poisson distribution.

3 Trigger concept, performances and alerts

At a given point in time, the particles within a shower front tend to align approximately in a spatial plane.

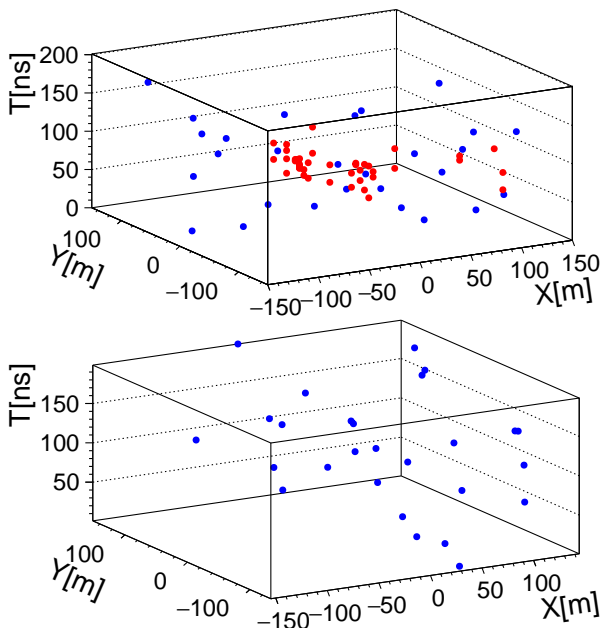


Fig. 4 (top) A signal event with 19 hit stations (red points) is superposed with 30 background stations (blue points) in a time window of 200 ns – the shower plane is trivially seen. (bottom) A background event with 27 hit stations (blue points)- no evidence for a shower plane is found.

When the shower front reaches the ground, this plane can be reconstructed using the spatial coordinates and arrival times of the impacted stations. In contrast, no such correlation exists among particles resulting from the superposition of tens of low-energy cosmic rays arriving randomly at the ground within the same time window. These distinctions are visually depicted in Fig. 4.

Three points in the space define one plane, which can be characterized by its normal vector. The combination of any three triggered stations defines thus a plane and its associated normal vector is designated as \mathbf{N}_i . When combining all the \mathbf{N}_i components in a single shower event, a distinct direction is indicated. Such would not happen for a background event coming from the superposition of tens of low-energy cosmic rays.

As an illustration, in Fig. 5 are shown the polar, θ , and azimuthal, ϕ , angles histograms of the directions of \mathbf{N}_i vectors in a signal (top) and a background event (bottom). The (θ, ϕ) histograms were constructed using the partition of the sky semi-hemisphere into 1000 equal-area cells using the prescription detailed in [16]. A clear peak is seen in the signal event, while no such peak is observed in the background event.

However, in the case of background events, there is a notable accumulation of data points in the vicinity of the vertical direction, as depicted in Figure 6. It is important to note that this phenomenon is primarily

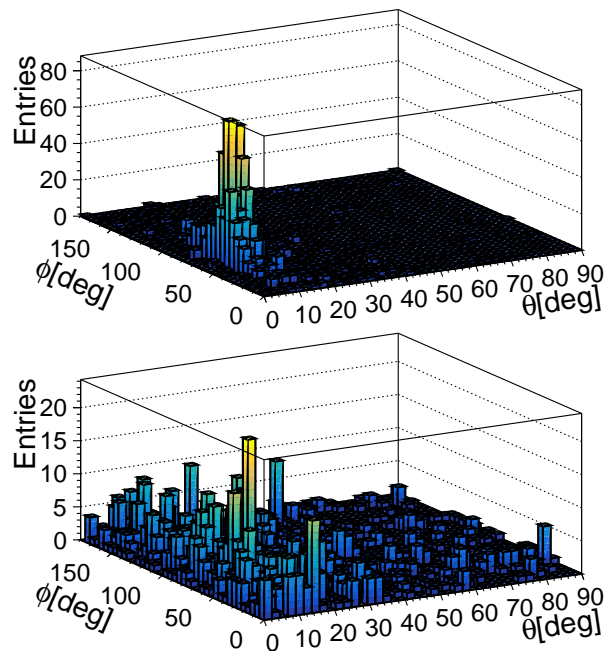


Fig. 5 Distribution of the directions of \mathbf{N}_i vectors in the plane (θ, ϕ) for a signal event with an energy of 55 GeV, polar angle 10° and 23 hit stations in a 200 ns time window (top) and for a background event with 19 hit stations in a 200 ns time window (bottom).

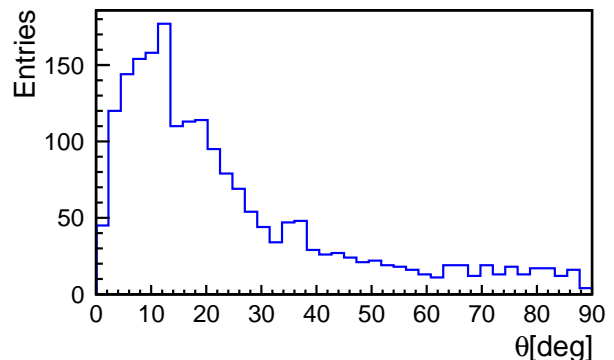


Fig. 6 Distribution of the directions of the \mathbf{N}_i vectors as a function of the zenith angle (θ) for a background event with 25 hit stations in a time window of 200 ns.

influenced by the length of the time window rather than the number of stations registering hits.

This consistent modulation of the θ angles in the directions of the background vectors \mathbf{N}_i has been examined as a means to perform a mean subtraction of the expected background, effectively mitigating potential small biases in θ . The results of this operation are illustrated in Figs. 7 and 8, for instance. The vacant bins within the *sky semi-hemisphere* in these figures result from an overestimation of the background, but this does not significantly affect the much higher signal cells.

Once we have arrived at the sky semi-hemisphere plots, created with the 3-station normal plane vectors, \mathbf{N}_i , and the removal of zenith background modulation, the final step is to determine the direction of the shower. Such was done by applying a QCD-based jet clustering algorithm to the cells content. Such jet algorithms are commonly used in Particle Physics for QCD studies (e.g [17]). To reconstruct the gamma-ray direction from the \mathbf{N}_i binned in a semi-hemisphere plane, a Cambridge-Aachen algorithm was used [18,19]. The method was adapted to reconstruction jets in a sky semi-hemisphere. For that the input coordinate system was changed for collider variable, namely pseudo-rapidity, η , was considered as a proxy for the polar angle, θ , and the azimuthal angle, ϕ , taken directly from the sky-coordinate system. Finally, the transverse momentum of each cell is taken as the number of hits in each station. As such, the sky hemisphere coordinate $(\eta, \phi) = (0, 0)$ was set to match the $(y, \phi) = (0, 0)$ in the collider coordinate system. Moreover, the jet radius was set to $R = 0.3$ (corresponding to 20°). All these steps were performed using the FastJet v.3.3.0 package [20]. The algorithm extracts the direction (θ, ϕ) of the gamma-ray shower from the reconstructed leading jet. This is to be understood as the axis of the jet that has higher number of combinations. The content of the sky bin corresponding to this direction serves as the event trigger variable, denoted as C_3^N . Additionally, this variable incorporates the count of combinations previously excluded from the same bin to effectively neutralize the zenith angle modulation introduced by background sources.

As an example, the polar (θ, ϕ) histograms of the direction of the jet vectors found in one gamma event (Fig. 7) and one event with one gamma and one proton (Fig. 8) superimposed to a mean atmospheric muon background. The colour scale represents the size of the vectors in each histogram cell.

When the value of C_3^N exceeds a specified threshold, denoted as C_3^{NT} , the event is triggered.

The value of C_3^{NT} determines the atmospheric background rejection factors as it is shown in Fig. 9. In this figure, displayed as a function of the value of $\log(C_3^N)$, it is shown the efficiency curve for atmospheric background events (black line), as well as the efficiency curves for gammas (blue) and protons (red) with primary energies of about 50, 80, 130 and 200 GeV. If C_3^{NT} is set to 1000 (1500) atmospheric background rejection factors higher than 10^3 (10^5) will be attained.

The trigger efficiencies, with C_3^{NT} set to 1000 and 1500, are presented in Fig. 10 as a function of the shower energy, for both gamma (blue line) and proton (red line) events. The shower events are embedded on the expected atmospheric background. An efficiency

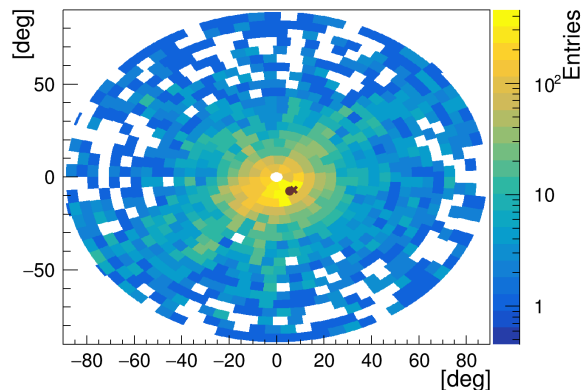


Fig. 7 Sky semi-hemisphere histogram of the direction vectors arising from the 3-station planes for a single event. This particular event is composed of: one gamma event with energy of $E_\gamma = 159.8$ GeV, $\theta = 10^\circ$ and $\phi = -43.2^\circ$; superimposing a mean atmospheric background event. The color scale represents the size of the combination vectors in each histogram cell. The black cross represents the original direction of the primary gamma and the black spot the reconstructed direction of the most prominent jet (see text for details).

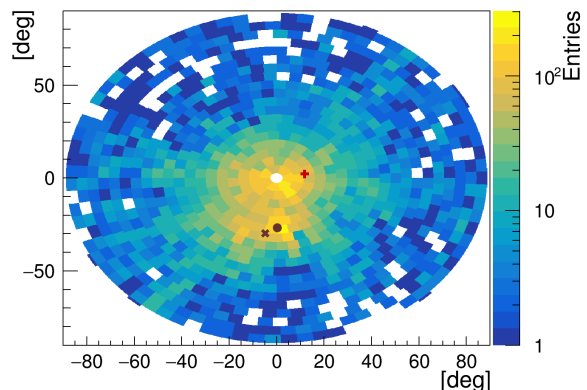


Fig. 8 Sky semi-hemisphere histogram of the direction vectors arising from the 3-station plane for a single event. This particular event is composed of: one gamma event with $E_\gamma = 45.5$ GeV, $\theta = 30^\circ$ and $\phi = -99.1^\circ$; one proton with an energy with $E_p = 155.5$ GeV, $\theta = 12.1^\circ$ and $\phi = 9.9^\circ$; and superimposing a mean atmospheric background event. The color scale represents the size of the combination vectors in each histogram cell. The black cross represents the original direction of the primary gamma and the black spot the reconstructed direction of the most prominent jet (see text for details). The original direction of the proton shower is given by a red cross.

rate of 10% corresponds to gamma events with energies around 50 GeV and proton events with energies of approximately 150 GeV. The proton curve exhibits a flattening at lower energies, which can be attributed to the thresholds set for atmospheric events, at 10^{-3} or 10^{-5} .

On the other hand, the angular accuracy of the tagged events as a function of the shower energy is

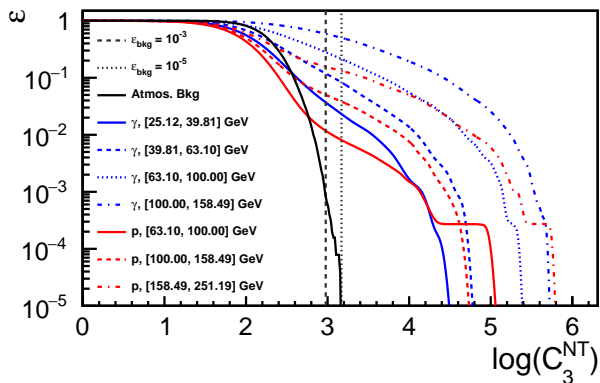


Fig. 9 Efficiencies curves as a function of $\log(C_3^{NT})$ for atmospheric background events (black line), as well as, the efficiency curves for gammas (blue) and protons (red) for different energies (see legend for details). The vertical dashed (dotted) black line represents the value of $\log(C_3^{NT})$ needed to ensure atmospheric background rejection factors of 10^{-3} and 10^{-5} .

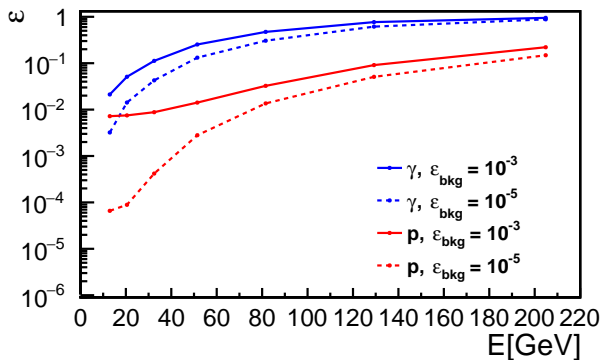


Fig. 10 Trigger efficiency as a function of the shower energy for gamma (blue line) and protons (red line), with the trigger threshold set at $C_3^{NT}=1000$ or $C_3^{NT}=1500$, corresponding to atmospheric background rejection factors of respectively $\epsilon_{\text{bkg}} = 10^{-3}$ and $\epsilon_{\text{bkg}} = 10^{-5}$.

shown in Fig. 11, setting C_3^{NT} to 1000. Even for energies as low as a few tens of GeV, a reasonably high angular accuracy within a few square degrees is assured. The proton lines are not displayed for energies below 80 GeV because the limited number of signal stations at the ground leads to a complete domination of these events by the background, rendering the results meaningless.

Efficient and timely management of alert reception and issuance has become an imperative aspect in the design of trigger systems for wide-field gamma-ray observatories. When an external alert is received, it becomes necessary to temporarily relax trigger requirements, allowing for the capture of the maximum possible number of events originating from the region in the sky associated with the alert. Conversely, when the observed events from a specific sky region meet predefined criteria in terms of their number or characteristics, alerts

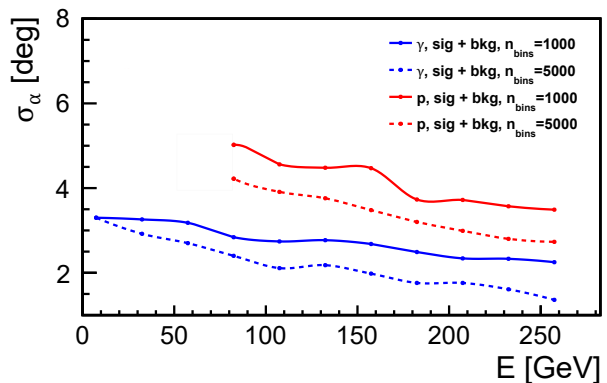


Fig. 11 Angular accuracy of gamma (blue line) and proton events as function of the energy of the primary gamma. See text for details.

should be disseminated to the global network of Astrophysics Observatories, all while maintaining a stringent standard to minimize the occurrence of false alerts.

A typical example of the necessity to issue fast alerts is the one connected with the investigation of VHE emission from Gamma-Ray Bursts (GRBs), where the onset of the VHE signal has a critical role in the interpretation of the mechanisms at play. GRBs have now been firmly detected in the VHE domain [21,22], but the frequency and the onset of this spectral component still needs to be understood [23]. To illustrate the performance of the trigger strategy discussed above, we can estimate the significance of an event with the spectral and temporal properties of GRB 130427A, using the same modelling strategy of [24]. The expected energy-dependent GRB and cosmic-ray rate counts in $80\,000\text{ m}^2$ were convolved with the corresponding trigger efficiencies. For the cosmic-ray background, only the fraction of events in a solid angle with a 3° semi-aperture were considered. This is a fair approximation of photon angular resolution reported in Fig. 11. As shown in Fig. 12, a 3σ significance level for such an event would be reached in just 2 seconds of integration time.

The impact of this trigger strategy can be further assessed by replicating the study of GRB detection prospects detailed in [24]. The possibility to detect VHE from GRBs, indeed, depends on three main factors: the GRB brightness (intended as the overall number of emitted photons); the GRB spectral hardness (affecting the likelihood of producing high energy photons); and the GRB redshift (which controls the VHE photon survival chances to $\gamma\gamma$ pair-production processes). By taking into account the difference in the involved spectral windows ($E \geq 125\text{ GeV}$ in [23], while $E \geq 10\text{ GeV}$ in this work), we can expect that the trigger strategy discussed here is more effective in the detection of high-

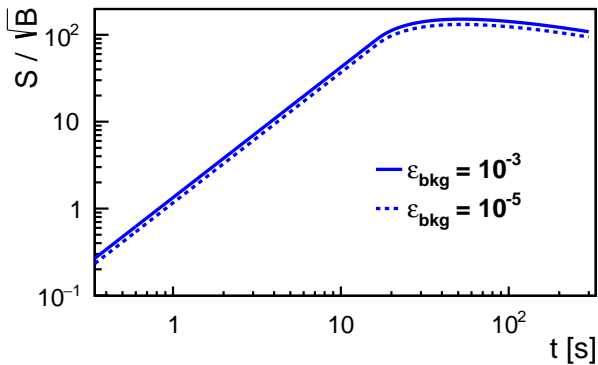


Fig. 12 Significance of the signal from GRB 130427A as a function of the integrated time, with the trigger threshold set at $C_3^{NT}=1000$ or $C_3^{NT}=1500$, corresponding to atmospheric background rejection factors of respectively $\varepsilon_{bkg} = 10^{-3}$ and $\varepsilon_{bkg} = 10^{-5}$. See text for more details.

redshift events, although the increase of the average redshift of detectable GRBs is counter-balanced by the requirement of a higher intrinsic source power (to keep the flux distribution consistent with the observed one) and, therefore, by a relatively lower number of potentially detectable events per unit volume. This effect can be appreciated in Fig. 13, where we show the distribution of possible GRB detections predicted by simulating 100 random redshift determinations for the 140 GRBs with unknown redshift detected by Fermi-LAT in 10 years of observation [25], in the assumption that they have power-law energy spectra suppressed by $\gamma\gamma$ opacity effects. For comparison, the figure also shows the corresponding distribution of the fraction of potentially detectable events obtained by [23] by integrating the expected GRB fluxes above 125 GeV. The new approach leads to a clear improvement. We have also observed that employing a background suppression level of $\varepsilon_{bkg} = 10^{-5}$ is expected to yield slightly better performance compared to the case of $\varepsilon_{bkg} = 10^{-3}$, particularly in terms of predicted detection numbers. However, it is worth noting that the latter case is more responsive to bright events like GRB 130427A, as illustrated in Fig. 12. This phenomenon may stem from the fact that the $\varepsilon_{bkg} = 10^{-5}$ setting can detect events that are marginally fainter but occur more frequently, albeit requiring approximately 10% longer integration times. It is important to emphasize that this difference is relatively modest, as evidenced by the case of GRB 130427A.

The sensitivity of such trigger strategy to issue alerts is further discussed in section 5.

This strategy to select signal events and to handle alerts, has obviously to be implemented on-line (see section 4) being able to deal with the fast increase of the total number of normal vector, n_{vec} , with the in-

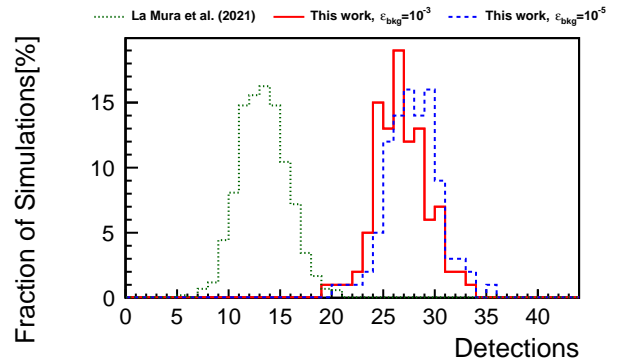


Fig. 13 Fraction of simulated GRB redshift distributions that would result in the reported number of detectable GRBs, from the population of 140 events with unknown redshift observed by *Fermi*-LAT in 10 years. The plot illustrates the improvement of the number of expected detections with the approach of this work for $\varepsilon_{bkg} = 10^{-3}$ (red histogram) and $\varepsilon_{bkg} = 10^{-5}$ (blue/dashed histogram) with respect to observations limited by a lower energy threshold of $E_{low} = 125$ GeV (green/dotted histogram).

crease of the number of hit stations ($n_{vec} = n_{hit}(n_{hit} - 1)(n_{hit} - 2)/6$)². This is the subject of the following section.

4 Hardware implementation

The computation of the \mathbf{N}_i vectors can be done by exploring a parallel computing architecture based on an FPGA-microprocessor system. Indeed, such types of solutions are becoming widely spread. For instance, a considerable effort is being made by Intel[®] in this direction.

In Fig. 14, a possible architecture of the trigger system is shown. Each station is continuously taking data, and a station-level trigger, T1, is generated each time the station registers a signal above the electronic noise. The information of the T1 is transmitted to the Central Unit Network Trigger and kept in a pipeline (station ID, space and time coordinates). Each 100 ns, the various T1 that have arrived in the last 250 ns are transferred to a buffer memory. If the number of T1 transferred to the buffer is higher than a given threshold (of about 70), a high multiplicity trigger is generated, activating the T2. Otherwise, the trigger will be handled by the *Low Energy Trigger* branch.

The Low Energy Trigger branch is composed of a large set of n trigger modules to compute, in parallel, the normal vectors \mathbf{N}_i of each event, and also a set of CPUs to handle, in parallel, the jet clusterization of computed \mathbf{N}_i vectors in each candidate event and,

²For instances, for $n_{hit} = 10$, $n_{vec} = 120$, while for $n_{hit} = 50$, $n_{vec} = 19600$.

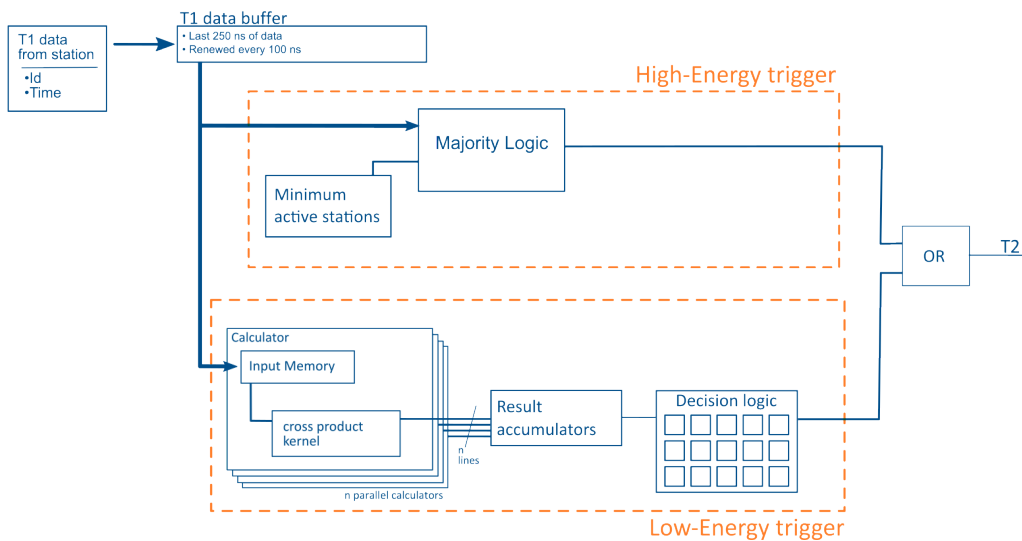


Fig. 14 Simplified scheme of a possible architecture of the trigger system. The low-energy trigger final decision is computed in a decision logic array that can be implemented as a CPU farm.

finally, to take a decision whether the event should be accepted or not.

Each trigger module is formed by an input memory, which is a mirror of the input buffer, and a calculator. All the modules' input memories are loaded in parallel. The calculator of each module computes the normal to the plane defined by a particular set of three T1 stations. These stations correspond to specific hard-coded positions of the module input memory. If the number of stations in the buffer is 70, there are $\sim 54\,700$ different combinations of 3 stations to be processed by the n modules, which are implemented using FPGAs.

The direction angles of the \mathbf{N}_i vectors of one event, computed by the calculators, are accumulated in a histogram kept in a memory array, which the cluster of CPUs may access. Each CPU will sequentially take care of one event, running the clusterization algorithm and taking the trigger final decision on that event.

To gain insight into the resource requirements for implementing the calculators of the trigger modules using an FPGA system, we implemented a basic algorithm in the Quartus suite by Intel using Verilog. This was done on a mid-low range FPGA and compiled without any optimizations. The resource allocation for this implementation involved 112 logic elements (ALMs) and 12 DSP blocks, all implemented using asynchronous logic. It is worth noting that the desired high level of parallelization can be readily achieved with high-range FPGAs.

Additionally, Intel is going to release the AGILEX family dedicated to intensive computations. It is then possible to implement in one of these FPGAs around 2000 calculators and, using a system of 10 Stratix FP-

GAs, up to 80 000 external products can be calculated in 10 ns.

On the other hand, suppressing most empty histogram cells, the mean execution time of the jet sequential clusterization algorithm in one event is, considering a 2403.0 MHz CPU, about $10\ \mu\text{s}$. In this way, a cluster of a few tens of CPUs may handle trigger rates of a few MHz and thus comply, at a reasonable cost, with the expected signal rates of low energy events, which deposited a total electromagnetic energy at the ground equivalent to a 100 GeV proton.

5 Discussion and Conclusions

In the context of Gamma Ray Large Wide-Field Observatories, maintaining low energy thresholds is pivotal in gathering robust statistical data. This significance is underscored by its application in two crucial scenarios:

- Transient phenomena, like the VHE emission from GRBs and flares, following and issuing alerts;
- Extended sources – such as the Fermi bubbles – and diffuse gamma emission, enlarging the energy range of the satellite experiments.

This study suggests that upcoming wide-field gamma-ray observatories, such as the forthcoming Southern Wide-field Gamma-ray Observatory (SWGGO) [26], have the potential to operate with remarkably low energy thresholds, reaching levels as low as tens of GeV. This advancement could result in substantial background rejection factors ranging from 10^3 to 10^5 and achieve mean angular resolutions, even at the trigger level, at approximately 3 degrees. Such capabilities would enable

round-the-clock alert issuance and monitoring throughout the year, effectively functioning as a monitoring observatory and trigger instrument for the Cherenkov Telescope Array (CTA), as well as gravitational waves and neutrino observatory.

The hardware implementation proposed (as detailed in Section 4) should be regarded as an initial, foundational step to assess the feasibility of a cost-effective implementation using current technology.

For future developments in trigger systems, it's imperative to closely monitor advancements, particularly at facilities like the Large Hadron Collider, where new triggering systems are adopting similar approaches but at significantly higher levels of complexity, especially in terms of online tracking reconstruction. These algorithms are also at the heart of fields such as computer vision, automated robot navigation, and autonomous vehicle guidance systems, all of which are evolving rapidly.

Acknowledgements The authors wish to express their appreciation for the financial support provided for this work by FCT - Fundação para a Ciência e a Tecnologia, I.P., through project PTDC/FIS-PAR/4300/2020 and EXPL/FIS-PAR/0905/2021. P. C. is grateful for the financial support by FCT under UI/BD/153576/2022. L. A. is grateful for the financial support by FCT under 2021.03209.CEECIND. G. L. M. is grateful for the financial support by 1.05.01.01 Fundamental research in Astrophysics under contract n. INAF-OAC-12/2023.

References

1. J. Aleksic, et al., *Astron. Astrophys.* **540**, A69 (2012). DOI 10.1051/0004-6361/201118166
2. H. Abdalla, et al., *Astron. Astrophys.* **612**, A1 (2018). DOI 10.1051/0004-6361/201732098
3. B.S. Acharya, et al., *Astropart. Phys.* **43**, 3 (2013). DOI 10.1016/j.astropartphys.2013.01.007
4. A.U. Abeysekara, et al., *Astrophys. J.* **881**, 134 (2019). DOI 10.3847/1538-4357/ab2f7d
5. F. Aharonian, et al., *Chin. Phys. C* **45**(8), 085002 (2021). DOI 10.1088/1674-1137/ac041b
6. W. Hofmann. Impact of altitude and Cherenkov photon detection efficiency on the energy threshold of SWGO-like arrays. HAP-20-003
7. D. Heck, et al., FZKA-6019 (1998)
8. ALMA. URL <https://www.almaobservatory.org>
9. P. Assis, et al., *Astropart. Phys.* **99**, 34 (2018). DOI 10.1016/j.astropartphys.2018.02.004. [Erratum: *Astropart. Phys.* 101, 36–36 (2018)]
10. J. Allison, et al., *Nuclear Instruments and Methods in Physics Research A* **835**, 186 (2016)
11. Agostinelli, et al., *Nuclear instruments and methods in physics research section A: Accelerators, Spectrometers, Detectors and Associated Equipment* **506**(3), 250 (2003)
12. Allison, et al., *IEEE Transactions on Nuclear Science* **53**(1), 270 (2006). DOI 10.1109/TNS.2006.869826
13. A. Ferrari, et al., CERN-2005-010, SLAC-R-773, INFN-TC-05-11 (2005)
14. T. Böhlen, et al., *Nuclear Data Sheets* **120**, 211 (2014)
15. S. Ostapchenko, *Phys. Rev.* **D83**, 014018 (2011). DOI 10.1103/PhysRevD.83.014018
16. B. Beckers, P. Beckers, *Computational Geometry* (45), 275 (2012)
17. G.P. Salam, *Eur. Phys. J. C* **67**, 637 (2010). DOI 10.1140/epjc/s10052-010-1314-6
18. Y.L. Dokshitzer, G.D. Leder, S. Moretti, B.R. Webber, *JHEP* **08**, 001 (1997). DOI 10.1088/1126-6708/1997/08/001
19. M. Wobisch, T. Wengler, in *Workshop on Monte Carlo Generators for HERA Physics (Plenary Starting Meeting)* (1998), pp. 270–279
20. M. Cacciari, G.P. Salam, G. Soyez, *Eur. Phys. J. C* **72**, 1896 (2012). DOI 10.1140/epjc/s10052-012-1896-2
21. MAGIC Collaboration, *Nature* **575**(7783), 455 (2019). DOI 10.1038/s41586-019-1750-x
22. LHAASO Collaboration, *Science* **380**(6652), 1390 (2023). DOI 10.1126/science.adg9328
23. G. La Mura, U. Barres de Almeida, R. Conceição, A. De Angelis, F. Longo, M. Pimenta, B. Tomé, D. Miceli, *Galaxies* **9**(4), 98 (2021). DOI 10.3390/galaxies9040098
24. G. La Mura, U.B. de Almeida, R. Conceição, A. De Angelis, F. Longo, M. Pimenta, E. Prandini, E. Ruiz-Velasco, B. Tomé, *Mon. Not. Roy. Astron. Soc.* **508**(1), 671 (2021). DOI 10.1093/mnras/stab2544
25. M. Ajello, et al., *Astrophys. Journal* **878**(1), 52 (2019). DOI 10.3847/1538-4357/ab1d4e
26. R. Conceição, PoS **ICRC2023**, 963 (2023). DOI 10.22323/1.444.0963